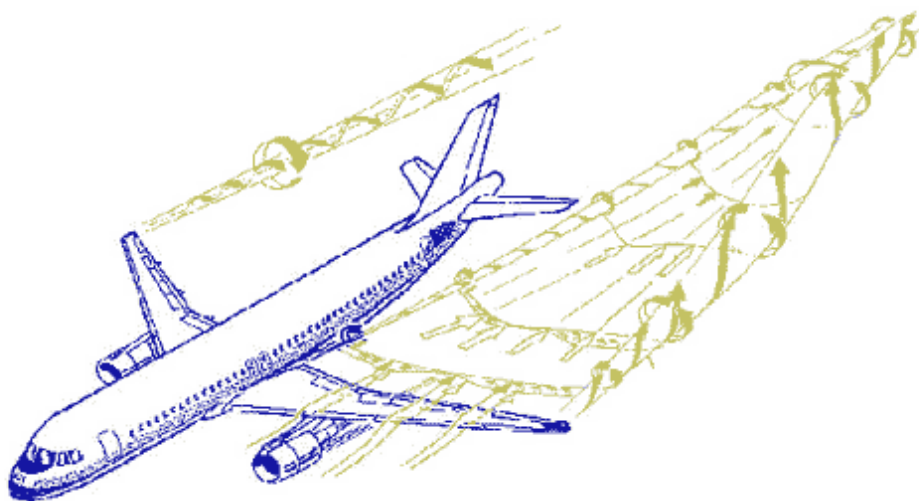


Effects of simple generic configuration on near to far field wake by using 3D Vortex Filament Method.

C-Wake Report UPS-PR 2.2.3-2

D. Margerit, P. Brancher and A. Giovannini

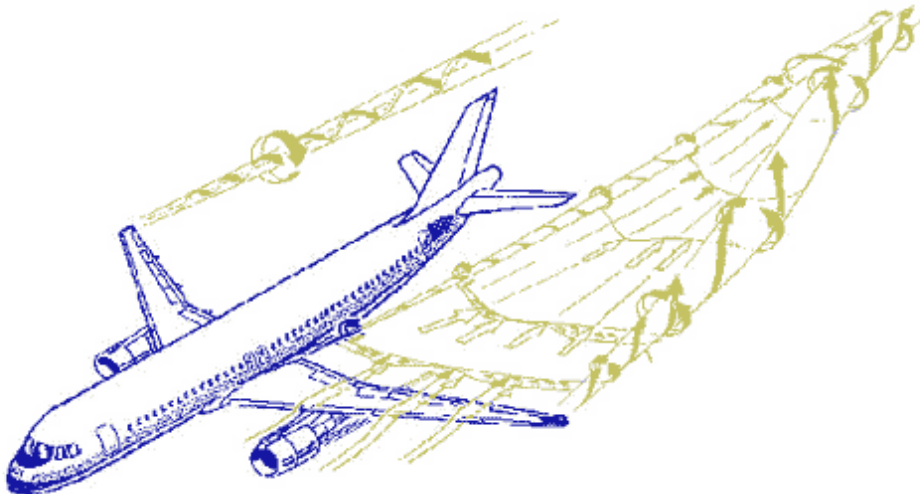
IMFT, Allée du professeur Camille Soula, 31400 Toulouse, France



C-Wake Project GRD1-1999-10332

Effects of simple generic configuration on near to far field wake by using 3D Vortex Filament Method.

C-Wake Report UPS PR 2.2.3-2



C-Wake Project GRD1-1999-10332

Prepared by: **D. Margerit, P. Brancher and A. Giovannini(UPS)**

Document control data

Deliverable No. :	PR 2.2.3-2	Approved by D. Darracq (Cerfacs)
Work Package:	WP 2.2.3	Reviewed by:
Version:	1	F. Laporte (Cerfacs)
Date of issue:	28-02-2002(month 25)	

I. INTRODUCTION

The potential hazard related to the two-vortex aircraft wake induces separation distances between aircrafts and associated delay at landing and take-off, which contributes to the congestion of airports [1–3]. Present ICAO separation rules in forces are conservative to minimize the risk of a possible wake encounter. Separation distances -based on aircraft weight- are empirical.

It was therefore considered indispensable to address, within the 5th Framework Program of the EC, the Wake Vortex Characterization and Control. The C-Wake project addresses the three following aspects: i) the physical aspects of a wake through wake characterization; ii) it produces application guidelines for the European aircraft industry on how to control the wake vortex size and intensity; iii) it synthesizes findings in order to arrive at a validated method of predicting a Large Transport Aircraft-Type's wake characteristics with sufficient accuracy.

As to better understand the interest of our work in subtask 2.2.3 of this project, it may be interesting to sketch a quick overview of the C-Wake organization. The C-Wake project consists of experimental work (Work Package 1 [WP1]), numerical and theoretical work (WP2) and a synthesis task (WP3) as can be seen in Fig. 1. WP2 consists of numerical computation of the near field (Task 2.1), far field extrapolation of near field result and prediction (Task 2.2) and theoretical study of unsteady effects (Task 2.3). Task 2.2 studies the effect of modifications to generic wing on far field wake (Subtask 2.2.1), the effect of design modifications to Airbus-type aircraft wing on wake (Subtask 2.2.2) and the configuration assessment by simplified methods (Subtask 2.2.3).

We are the only one in subtask 2.2.3 who use a fully 3D method. Our goal is to study the effect of a simple geometric configuration on near to far field wake by using 3D vortex filament methods. As it was defined in the C-Wake initial Project [4], our work is in four steps: i) adaptation of a vortex filament method, ii) acceleration of the method, iii) validation and iv) parametric study. It lasts from the middle of March 2000 to the end of February 2002.

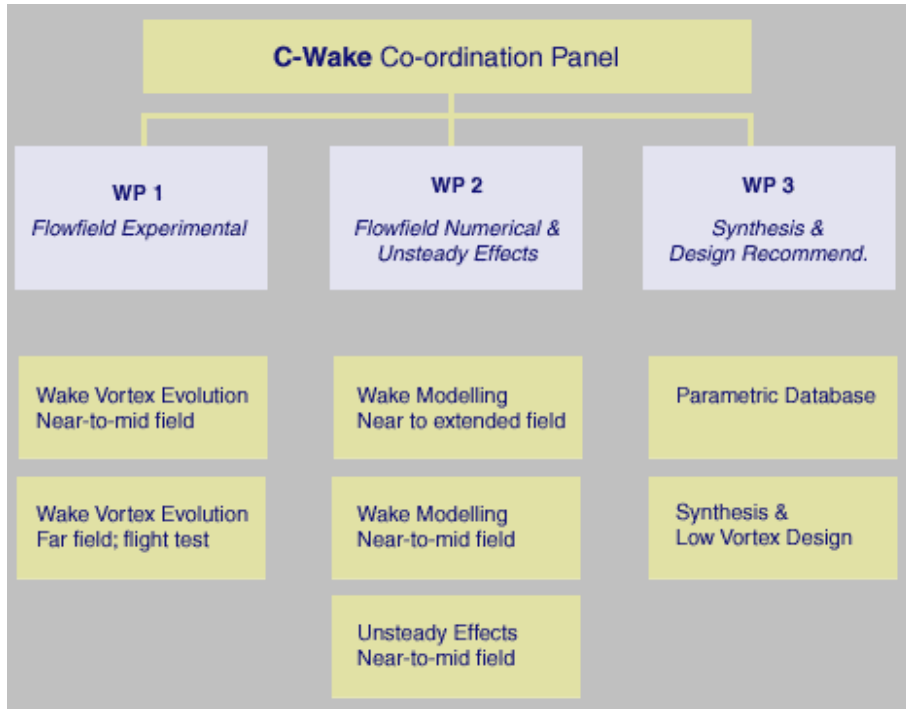


FIG. 1. C-Wake organisation

Vortex methods [5–8] are numerical methods of great interest to study *vortical flows*. The discretization is of the vorticity field, rather than the velocity field, and is Lagrangian in nature. It consists of a collection of particles (Vortex Particle methods [VP]) or filaments (Vortex Filament methods [VF]) which carry concentrations of vorticity. The velocity field is recovered from the discretized vorticity field via the Biot-Savart law and a *numerical smoothing parameter* is introduced to desingularize the Biot-Savart line-integral kernel. The vorticity field is then evolved in time according to this velocity field.

We have implemented [9] a *slender* vortex filament (SVF) code based on asymptotic equations of motion [10–12] derived by Callegari and Ting from the Navier-Stokes equations in the slenderness limit. For a closed vortex let us briefly introduce this equation which is the heart of our work. A *slender vortex ring* of circulation

filament at time t . The growth rate is given by the slope of the temporal function $\log[\rho(s, t)/\rho(0)]$. It converges with all numerical parameters (time step, number of points and number of boxes) and with decreasing initial amplitude ρ_0 . With an axial flux ($m_0/\Gamma \neq 0$) the ε axis of the previous figures is multiplied by $\exp(-2[m_0/\Gamma]^2)$. We checked that analytical and numerical results also agree for $m_0/\Gamma = 0.6$.

Figure 6 displays the evolution of the Crow instability of the most unstable mode in the non-linear regime (Run 8 in Table I). For sake of clarity the curve of the centerline is represented by a tube with an arbitrary core radius.

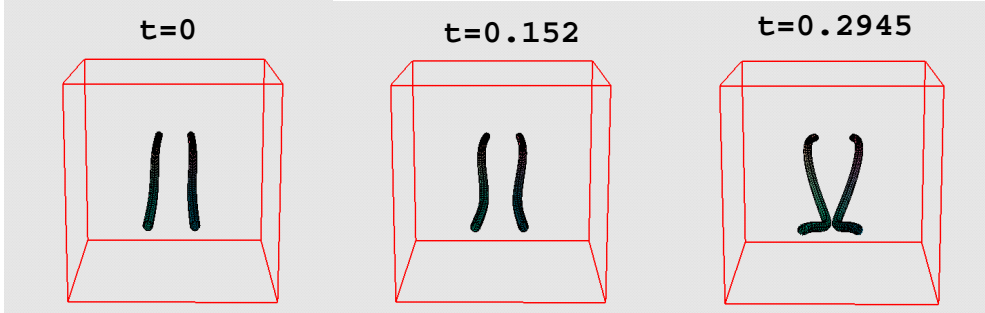


FIG. 6. Vortex Filament Simulation of the non-linear instability regime of the most unstable mode $\Lambda = 10.21$ for the contra-rotating vortex pair. Initial amplitude $\rho = 0.05$, initial thickness $\varepsilon = 0.02$ and initial angle $\theta(t = 0) = 47.63(\text{deg})$.

Viscous and non-similar effects are implemented in EZ-vortex but could not be validated by lack of known analytical results. The linear growth rate β found from the first time steps as before is almost constant with the viscous parameter $\bar{\nu} = \nu/\varepsilon^2$ till $\bar{\nu} \simeq 4$. The maximum amplitude on the filament $\rho(t)$ as a function of time is weakly affected by the viscosity ($\bar{\nu} = 1$) in the non-linear regime. The simulations of the Rankine or the *witch-hat* profiles (see Appendix B) give almost the same maximum amplitude $\rho(t)$ evolution as for a similar core.

B. Study of a four-vortex aircraft wake

In this subsection the EZ-vortex code is used to study a four-vortex aircraft wake. It gives a last validation of the code. As in the previous section all following simulations use the M1 de-singularized method of Knio and Klein with the explicit Adams-Bashforth scheme, there is no axial flow ($m_0 = 0$) and the fluid is inviscid ($\bar{\nu} = 0$). Here, the vortex core is a *Rankine* profile. The two trailing vortex pairs have the same axis of symmetry. Let us denote $\Gamma_o, \Gamma_i, L_o, L_i, \bar{\delta}_o(t = 0)$ and $\bar{\delta}_i(t = 0)$ the circulations, the distances and the thickness of the outer and inner vortex pairs. We introduce the dimensionless parameters $R = L_i/L_o$ and $G = \Gamma_i/\Gamma_o$. The initial outer reduced thickness is $\bar{\delta}_o(t = 0) = 1$ and so the small parameter ε is the initial thickness of the outer pair.

TABLE II. Four-vortex modes: linear stability (th.) and EZ-vortex (num.) results at $\varepsilon = 0.1$.

	Λ	β	$\theta_o(\text{deg})$	$\theta_i(\text{deg})$	$\varrho = \rho_i/\rho_o$
Most amplified S1 mode (th.) [18]*	0.8976	2.91	105.86	131.24	57.4
" (num. Run 9 in Table I)	"	2.94	111.04	130.20	52.8
Long-wave S1 mode (th.) [18]*	7.85	1.55	145.45	103.85	9.72
" (num. Run 11 in Table I)	"	1.56	145.68	103.73	9.80
Long-wave A mode (th.) [18]*	7.85	1.469	116.90	167.03	9.58
" (num. Run 11 in Table I)	"	1.511	118.72	166.39	9.73

*results given by D. Fabre.

There is an exact stationary solution of the equation of motion (B12) provided that the following relation between G and R is satisfied [20]

$$G = -\frac{3R + R^3}{3R^2 + 1}. \quad (6)$$

The associated velocity V is

$$V = \frac{\Gamma_i}{2\pi L_i} + \frac{2\Gamma_o}{\pi L_o} \frac{1}{1 - R^2}. \quad (7)$$

We checked that the **EZ-vortex** code reproduces this velocity for the ratio $R = 0.14$ (associated G is -0.4 .) used by Fabre and Jacquin [18].

As for the contra-rotating vortex pair sinusoidal unstable modes exist. The growing perturbations are planar with planes fixed at angles θ_o (outer trailing pair) and θ_i (inner trailing pair) with respect to the horizontal [18]. Let $\varrho = \rho_i/\rho_o$ be the ratio of the amplitudes. Fabre and Jacquin [18] carried out the linear stability study of this wake and gave results for $R = 0.14$ ($G = -0.4$), $\varepsilon = 0.1$, $\bar{\delta}_o(t = 0) = 1$, $\bar{\delta}_i(t = 0) = 0.5$, $\Gamma_o = 1$ and $L_o = 1$. The growth rates and the associated modes of the most amplified S1 mode $\Lambda = 0.8976$ and for the long-wave S1 and A modes $\Lambda = 7.85$ are given in Table II. We have reproduced these results with the **EZ-vortex** code by starting from a perturbation amplitude $\rho_0 = 0.001$.

TABLE III. Four-vortex modes: linear stability (th.) at $\varepsilon = 0.02$.

	Λ	β	θ_o (deg)	θ_i (deg)	$\varrho = \rho_i/\rho_o$
Most amplified S1 mode (th.)*	1.2566	3.07	82.81	132.53	48.5
Long-wave S1 mode (th.)*	7.85	1.62	140.36	104.35	10.00
Long-wave A mode (th.)*	7.85	1.40	110.13	167.54	9.35

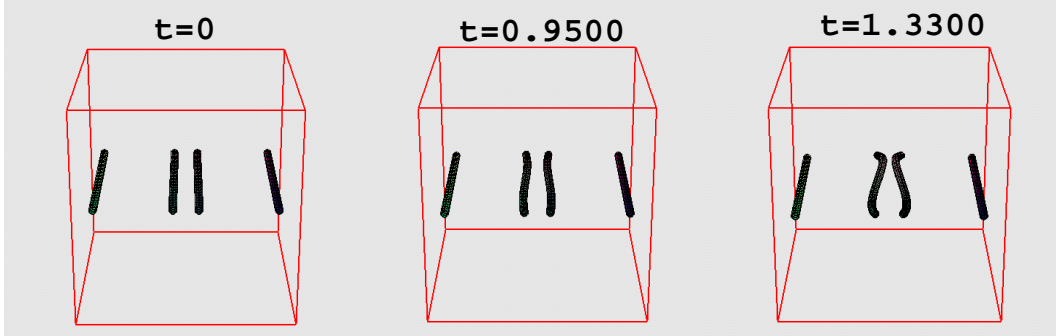
* results given by D. Fabre.

The growth rate β is obtained from the slopes of the temporal functions $\log[\rho_\alpha(s, t)/\rho_\alpha(0)]$ with the amplitudes $\rho_o(s, t)$ and $\rho_i(s, t)$ measured by

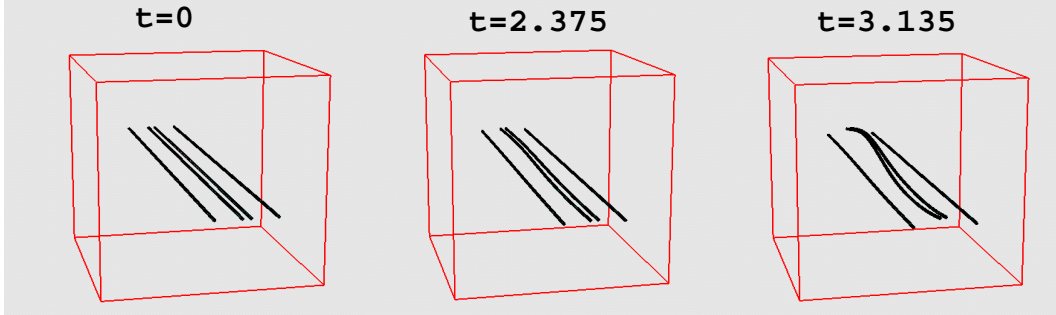
$$\begin{aligned} \rho_o^2(s, t) &= [Z_o(s, t) - \bar{Z}_o(t)]^2 + [Y_o(s, t) - \bar{Y}_o(t)]^2, \\ \rho_i^2(s, t) &= [Z_i(s, t) - \bar{Z}_i(t)]^2 + [Y_i(s, t) - \bar{Y}_i(t)]^2, \end{aligned} \quad (8)$$

where $\mathbf{X}_\alpha = (X_\alpha, Y_\alpha, Z_\alpha)$ and $\bar{Z}_\alpha(t)$ and $\bar{Y}_\alpha(t)$ are the spatial averages on the filament $\alpha = o$ or i at time t . We start with the linear stability results and carry out several computations starting with $\rho_0 = 0.001$ and with $(\theta_o, \theta_i, \varrho = \rho_i/\rho_o)$ from the final values of previous computation. It converges to fixed values reported in Table II. We have carried out the same comparison for $\varepsilon = 0.02$ and shown that the small difference between numerical and linear stability results disappears (Table III). This difference is thus due to finite ε effects. Figure 7 displays the evolution of these modes in the non-linear regime. The numerical parameters of the computation are given in Table I (Runs 10 and 12).

Most amplified S1 mode $\Lambda = 0.8976$.



Long-wave S1 mode $\Lambda = 7.85$.



Long-wave A mode $\Lambda = 7.85$.

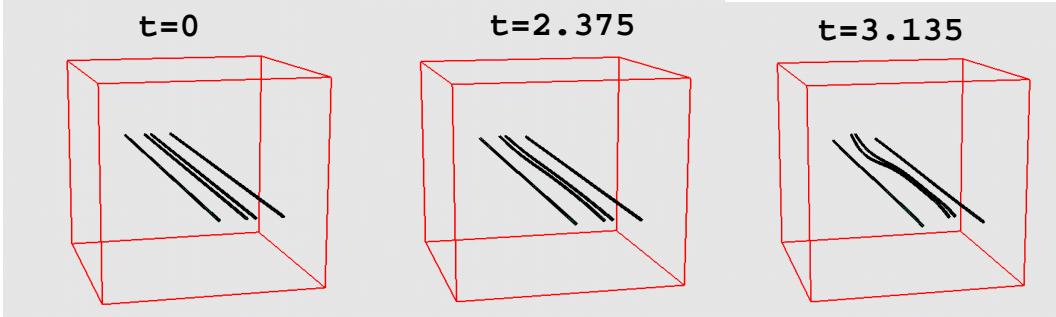


FIG. 7. Vortex Filament Simulation of the non-linear instability regime of typical modes for the four-vortex wake. Initial amplitude $\rho_0 = 0.001$ and initial thickness $\varepsilon = 0.1$. (The visualization of the filaments uses equal core radius even if the computation uses unequal sizes.)

IV. ANALYSE OF WIND TUNNEL DATA

In this section we give a brief overview of the NLR experiments and results in wind tunnel on a generic model: the SWIM model geometry, and consist in 6 model configurations. We then complete the data analysis of NLR to find the physical parameters that we need as an input (initial condition) of our EZ-vortex computation. We first explain how we do the analysis and then give the parameters of the different runs to be done.

A. SWIM geometry and NLR experiments in LST and LLF wind tunnels

These experimental results are for a generic model: the SWIM model geometry, and consist in 6 model configurations. Fig. 8 gives the photos of these 6 configurations and Fig. 9 gives the dimension of the wing and the lateral position of the spoiler elements.

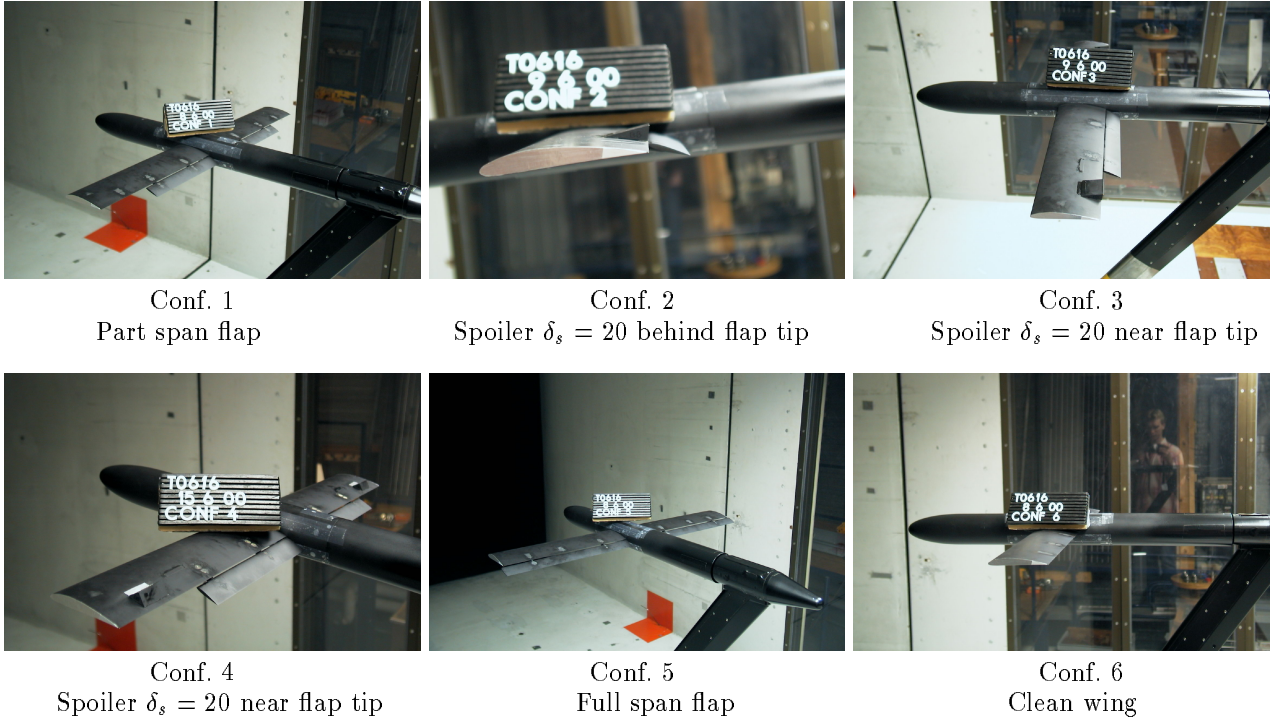


FIG. 8. The 6 model configurations [25]

B. Results and data analysis from NLR

The NLR CD-Rom [25] gives all the results for LST (PIV and Rake) and LLF tests. It consists of different ascii data files. They give the velocity components (over U_0) and the computed axial vorticity component on interpolated grids that cover all the flow field behind the wing. In these files there is a column for each component on the grid. The number of grid points in y and z directions changes from one file to one other and it is not given. In LST measurement PIV results are unable to give the velocity field inside the strongest vortices. For each data file the configuration number and the cross section position x/b can be found from Table 3a to Table 3f in the NLR report [26]. For example Fig. 11 gives the velocity and the vorticity fields that we plot with Matlab from the dat file *rake02022.dat* : rake data results for configuration 1 at $x/b = 5$.

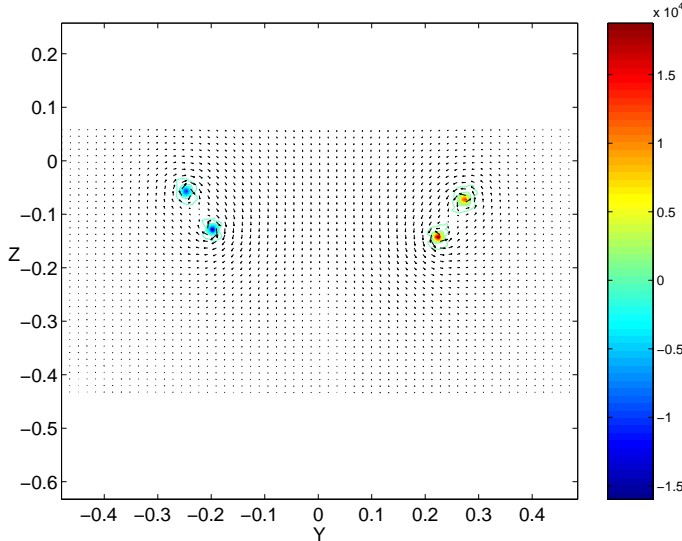


FIG. 11. Velocity field and axial vorticity contourplot for configuration 1 at $x/b = 5$ (file *rake021022.dat* [25])

In order to generate the initial conditions of the EZ-vortex code from these experimental data we need to have a physical analysis of the flow, i.e. to have the physical parameters: *number of vortices, their circulation, position and thickness*. The result of the data analysis of NLR can be found from Table 3a to Table 3f in the NLR report [26]. We can find from these tables the position of vortices and the total circulation on the left and right hand side of the wing. This circulation is found both by a surface integral of the vorticity field (Γ_s) and a line integral of the velocity field (Γ_c). For example for the run of Fig. 11 it gives: $\Gamma_s = -4.125 \text{ m}^2/\text{s}$ and $\Gamma_c = -4.125 \text{ m}^2/\text{s}$ on the left hand wing and $\Gamma_s = 3.937 \text{ m}^2/\text{s}$ and $\Gamma_c = 3.953 \text{ m}^2/\text{s}$ on the right hand wing. Unfortunately the number of vortices, their individual circulation and their core thickness are not given in these Tables. As we need it we have completed the analysis of NLR by computing these physical parameters for the different experimental data files.

C. Our analysis of the data files

We will present our analysis on the same run as in Fig. 11. We first find the center of the each vortex from Fig. 11 and select a circular domain around its center (Fig. 12).

We then interpolate the vorticity field on a polar grid around this circular domain and do the angular average of this field to obtain the radial velocity profile of vorticity (dot points in Fig. 13). As a Gaussian profile only depends on the circulation Γ and core thickness δ (see Appendix B), these two parameters can be found from an optimization routine to find the Gaussian profile that best fits the experimental one in the least square sense (Fig. 13). We use usual Matlab routines to develop this analyzer of the data files and made this program as automatic as possible. In the same way the amplitude of non-Gaussian moments (in the Laguerre series sense: see Appendix B) can be found.

We find that $\Gamma = -2.7014 \text{ m}^2/\text{s}$ and $\delta = 0.011 \text{ m}$ for the vortex in the circle of Fig. 12. Curiously rake vorticity field are divided by 100 as regard to corresponding PIV-LST vorticity (for example compare files *rake4301.dat* and *piv7501.dat*): we then have multiplied rake vorticity and PIV-LLF vorticity by 100. This procedure of finding the circulation is much more accurate than computing a surface integral of the vorticity

$(\Gamma = \sim -3.22 \text{ m}^2/\text{s})$ or a line integral of the velocity ($\Gamma = -3.5 \text{ m}^2/\text{s}$). The obtained thickness is also more accurate than the one obtained by using the computed circulation and the extremum of vorticity. The circulation on the left hand wing is $\Gamma = -4.903 \text{ m}^2/\text{s}$ and the one of the right hand wing is $\Gamma = 5.057 \text{ m}^2/\text{s}$ to be compared with the values of $\Gamma_s = 4.125 \text{ m}^2/\text{s}$ and $\Gamma_s = 3.937 \text{ m}^2/\text{s}$ found by NLR. We also can find the radial profile of $W - U_0$ and extract the axial flux m_0 in the vortex. We find that $M_0/U_0 = -0.00427 \text{ m}^2$ for the vortex in the circle of Fig. 12.

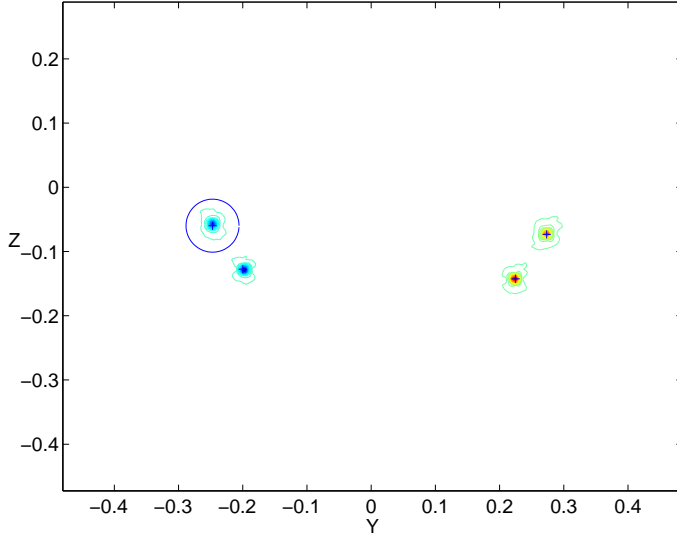


FIG. 12. Contour-plot of vorticity (same data file as Fig. 11). The circle is the domain of analysis of the associated vortex.

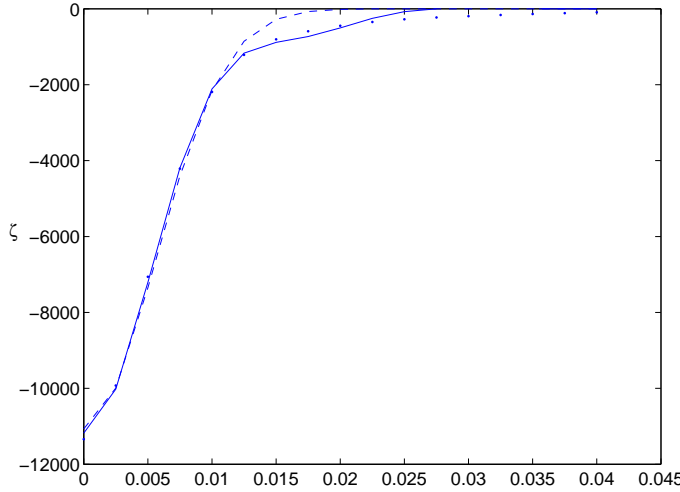


FIG. 13. Radial axial vorticity ζ profile of the vortex in the circle of Fig. 12. We show the experimental profile: dotted line, the best Gaussian profile: dashed line and the best non-Gaussian profile: solid line.

From the analysis of the positions of the vortices we can display the wake of the six configurations (Fig. 14). As can be seen from Fig. 14 there is no long wavelength 3D effect in these experiments. There is first a merging of the co-rotating filaments with either a 2D merging or a short wavelength instability merging and then a 2D motion of the resulting trailing vortices. As our code captures 3D curvature long wavelength effect, it is a useful tools to extrapolate these experimental mid field to the far field by using the last cross section velocity field. The last stage $x/b = 30$ of experimental data can be extended to 3D and we can carry out a temporal computation with EZ-vortex. In order to do this we need to extract the physical parameters from the different last cross sections.

TABLE VII. Numerical parameters: open vortices

Configuration	Λ	np	dt (s)	nb	nsteps	CPU time*(s)
1	4.8336	101	0.000285	8	7950	2542
2	4.7653	101	0.000285	8	7950	2551
3	4.7673	101	0.000285	8	7950	2558
6	5.8482	151	0.00038	8	11925	8548

*SGI R10000 work-station at 225MHz

The linear time is $t_l = 1/\beta$ where β is the linear growth rate. The result of the computations is given in Table VIII, where $t^* = t/t_0$ with $t_0 = 2\pi L^2/\Gamma$ [2].

TABLE VIII. Linear and collision times ($\rho_0 = 0.01$ (m), i.e. $\rho_0/L \sim 0.02$).

Configuration	t_0 (s)	t_l (s)	t_l^*	t_c (s)	t_c^*
1	0.42	0.50	1.19	1.67	3.97
2	0.39	0.47	1.21	1.55	3.98
3	0.27	0.33	1.22	1.14	4.22
6	0.8	0.93	1.16	3.04	3.8

Numerical computation of configurations 1, 2, 3 and 6 are given in Fig. 15-18.

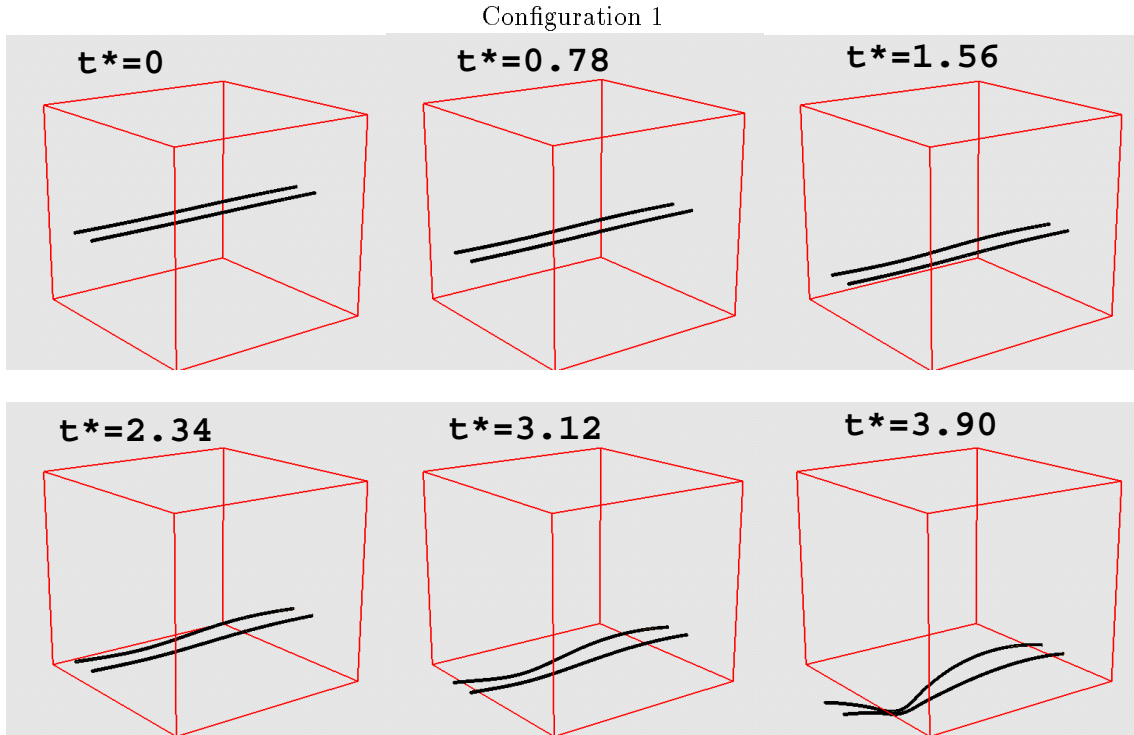


FIG. 15. Vortex Filament Simulation of the far wake for configuration 1.

Configuration 2

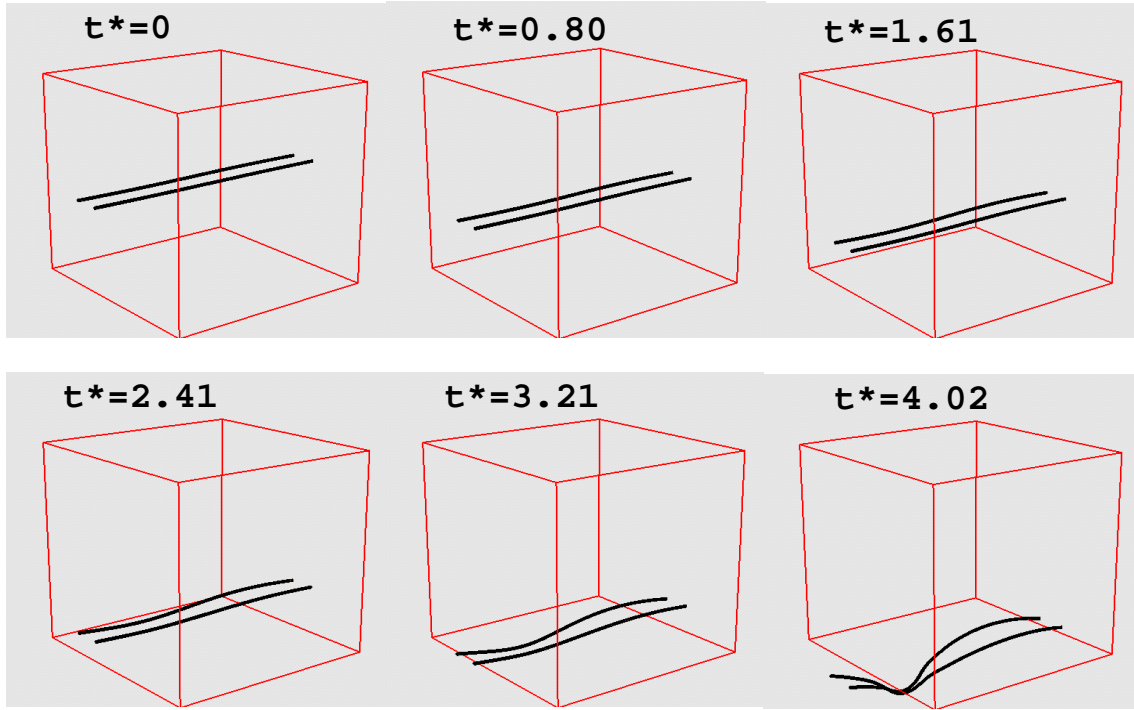


FIG. 16. Vortex Filament Simulation of the far wake for configuration 2.

Configuration 3

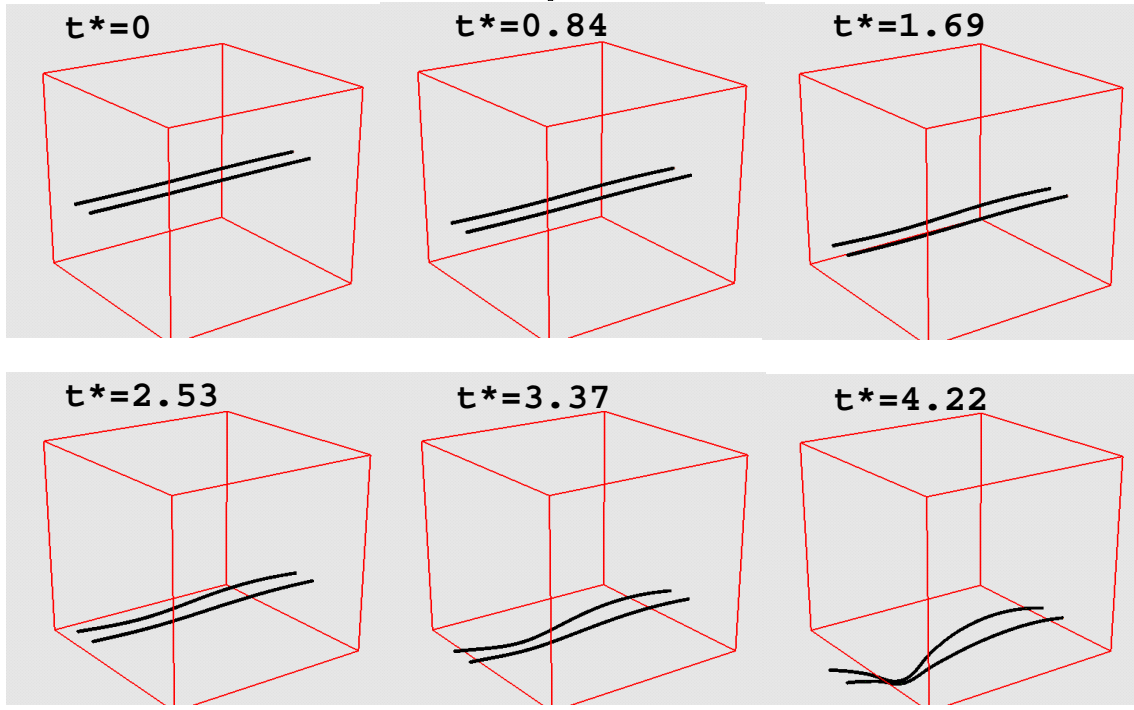


FIG. 17. Vortex Filament Simulation of the far wake for configuration 3.

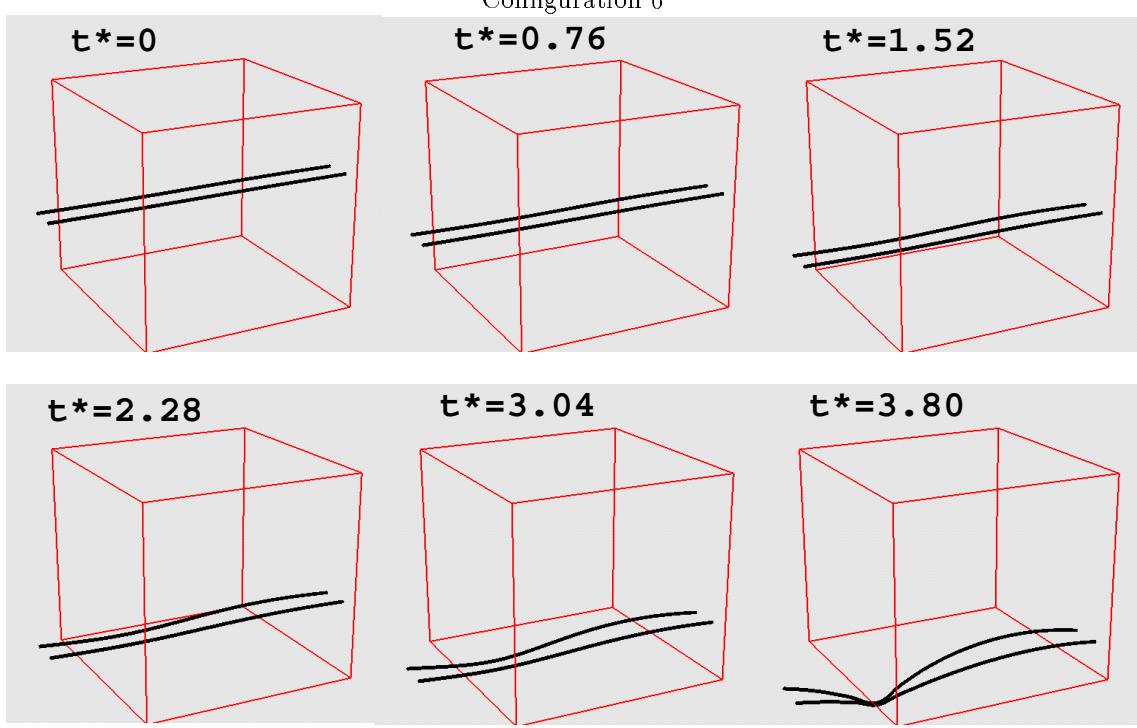


FIG. 18. Vortex Filament Simulation of the far wake for configuration 6.
Our main conclusions for this parametric study are as follow:

- For the 4 configurations the collision time is about 3.3 times the linear stability time ($t_c \equiv 3.3t_l$).
- In dimensionless form all simulations and collision time are almost the same.
- In dimension form configuration 3 is the quickest to reconnect the vortices.